ACS APPLIED MATERIALS & INTERFACES

Research Article

Cite This: ACS Appl. Mater. Interfaces 2018, 10, 35477−35486

www.acsami.org

Environmentally and Mechanically Stable Selenium 1D/2D Hybrid Structures for Broad-Range Photoresponse from Ultraviolet to Infrared Wavelengths

Yu-Ze Chen,[†,#,○] Yen-Ting You,[†,#,○] Pin-Jung Chen,[†,#] Dapan Li,[∥] Teng-Yu Su,[†,#] Ling Lee,[†,#] Yu-Chuan Shih,[†,#] Chia-Wei Chen,[†,#] Ching-Chen Chang,[†,#] Yi-Chung Wang,[†,#] Cheng-You Hong,[§] Tzu-Chien Wei,[§] Johnny C. Ho,[∥] Kung-Hwa Wei,[⊥] Chang-Hong Shen,[*,▽] and Yu-Lun Chueh[*,†,‡,#]

[†]Department of Materials Science and Engineering, Frontier Research Center on Fundamental and Applied Sciences of Matters, and [§]Department of Chemical Engineering, National Tsing Hua University, Hsinchu 30013, Taiwan, ROC

[‡]School of Materials Science and Engineering, State Key Laboratory of Advanced Processing and Recycling of Non-Ferrous Metals in Gansu Province, Lanzhou University of Technology, Lanzhou City 730050, Gansu Province, P. R. China

[#]Department of Physics, National Sun Yat-Sen University, Kaohsiung 80424, Taiwan, ROC

[∥]Department of Materials Science and Engineering, City University of Hong Kong, Kowloon 999077, Hong Kong S.A.R., P. R. China

[⊥]Department of Materials Science and Engineering and Center for Emergent Functional Matter Science, National Chiao Tung University, Hsinchu 30010, Taiwan, ROC

[▽]National Nano Device Laboratories (NDL), Hsinchu 30078, Taiwan, ROC

Supporting Information

ABSTRACT: Selenium (Se) is one of the potential candidates as photodetector because of its outstanding properties such as high photoconductivity (~8 × 10^4 S cm^{-1}), piezoelectricity, thermoelectricity, and nonlinear optical responses. Solution phase synthesis becomes an efficient way to produce Se, but a contamination issue that could deteriorate the electric characteristic of Se should be taken into account. In this work, a facile, controllable approach of synthesizing Se nanowires (NWs)/films via a plasma-assisted growth process was demonstrated at the low substrate temperature of 100 °C. The detailed formation mechanisms of nanowires arrays to thin films at different plasma powers were investigated. Moreover, indium (In) layer was used to enhance the adhesive strength with 50% improvement on a SiO_2/Si substrate by mechanical interlocking and surface alloying between Se and In layers, indicating great tolerance for mechanical stress for future wearable devices applications. Furthermore, the direct growth of Se NWs/films on a poly(ethylene terephthalate) substrate was demonstrated, exhibiting a visible to broad infrared detection ranges from 405 to 1555 nm with a high on/off ratio of ~700 as well as the fast response time less than 25 ms. In addition, the devices exhibited fascinating stability in the atmosphere over one month.

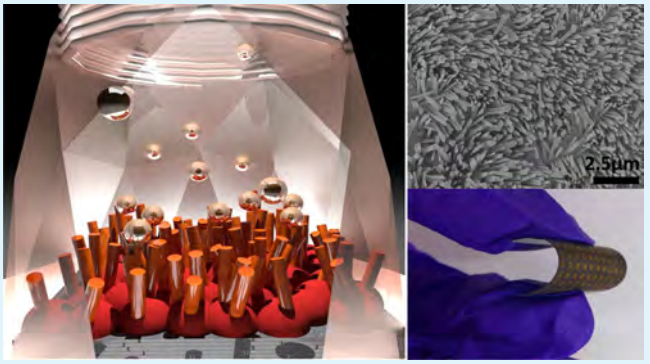

KEYWORDS: *Se nanowires arrays, plasma-assisted selenization process, flexible substrate, adhesion ability, broad-ranged photoresponse*

INTRODUCTION

Sensing behavior is the process of converting physical or chemical signals, including voice, temperature, pressure, humidity, length, and PH scales to recordable electronic signals.[1−4] Among those sensors, photodetectors have a wide variety of applications in our daily life, including fiber-optic communications, remote sensing, and charge-couple device inside a camera.[5] The main criteria of being a good photodetector include a high sensitivity at a designed operating wavelength with a high response speed, a large optical to electrical conversion efficiency, a large signal-to-noise ratio, a high reliability, and a low sensitivity to ambient conditions in performance.[6] Not only pursuing the high performance but also lowering the cost of manufacture is imperative to develop

Received: July 12, 2018
Accepted: August 14, 2018
Published: August 14, 2018

Downloaded via CITY UNIV OF HONG KONG on November 16, 2018 at 07:41:25 (UTC).
See https://pubs.acs.org/sharingguidelines for options on how to legitimately share published articles.

© 2018 American Chemical Society

DOI: 10.1021/acsami.8b11676
ACS Appl. Mater. Interfaces 2018, 10, 35477−35486

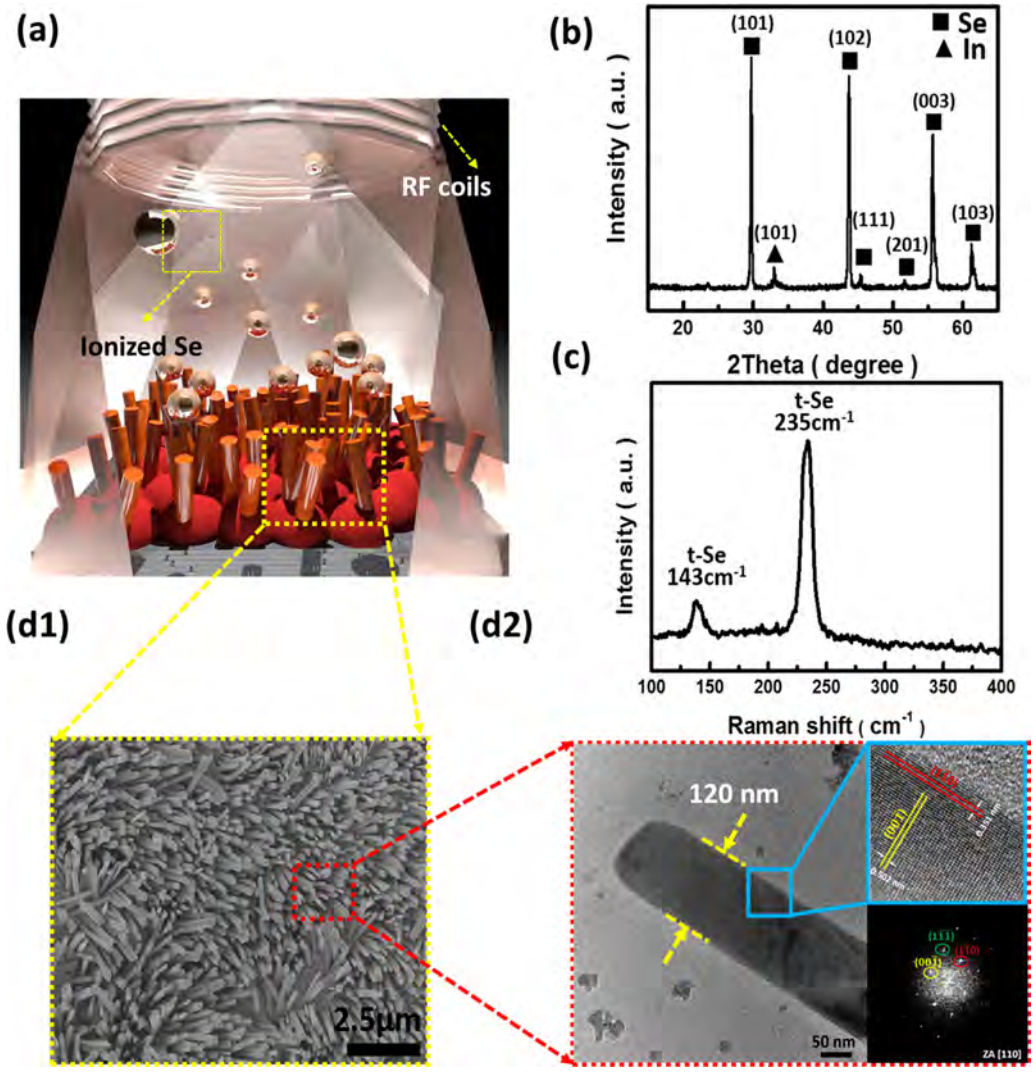

Figure 1. (a) Schematic of the plasma-assisted selenization process including Se source, plasma, and the heating stage. (b) The XRD diffraction patterns of Se/In structures. (c) Raman spectrum of the resulting Se/In structures displaying featured peaks of Se located at 143 and 235 cm^{-1}. (d1) A top view SEM image of Se NWs. (d2) A magnified TEM image of single Se nanowire confirms the growth direction of [110]. Inset displays a high-resolution transmission electron microscope (HRTEM) image with the lattice spacings of 0.351 nm of $(1\bar{1}0)$ and 0.502 nm of $(00\bar{1})$.

practical electronics. Among all materials, selenium (Se) possesses a wide variety of fascinating features, including high photoconductivity ($\sim 8 \times 10^4$ S cm^{-1}), superior spectral sensitivity, large piezoelectric, thermoelectric, and nonlinear responses.[7] The first Se-based photodetector can be traced back to 1873 when Smith discovered the phenomenon of photoconductivity using Se as the detecting material.[8] Up to date, Se had been extensively studied in many attractive fields such as biology and material sciences to commercial applications.[9]

Several approaches of preparing low-dimensional Se nanostructures such as nanoparticles and nanowires (NWs) have been reported.[10−15] Li et al. obtained Se NWs by reducing selenious acid with hydrazine hydrate in different solvents along with a sonochemical treatment.[16] Lu et al. demonstrated the formation of Se nanobelts by using cellulose as both the reducing and morphology-directing agent under hydrothermal conditions.[17] Xie et al. reported the Se nanotubes using SeO_2 and poly(vinylpyrrolidone) by a photothermal assisted method, although suffering from the chemical residues.[18] According to the aforementioned method, chemical reagents always get involved in the growth of these low-dimensional Se nano/microstructures, resulting in chemical contamination. Although the chemical approach can provide mass production at low cost, the contamination issue may hamper the further device application due to the poor crystallinity, surfactant absorption, and high density of defects.[19,20] Besides, the chemically synthetic process is time-consuming and not environmentally friendly owing to the use of toxic reagents.[14,21,22] Therefore, a simple, time-saving and environmentally friendly fabrication process to prepare low-dimensional Se nanostructures with high quality is imperative for practical applications.

In this regard, a reliable, low-temperature, and catalyst-free approach of synthesizing Se nanostructures from one-dimensional (1D) nanowires (NWs) arrays to two-dimensional (2D) thin films by tuning the growth parameter was demonstrated. The crystallinity, microstructures, and morphologies that evolved with different process parameters were investigated and characterized by Raman spectrum, scanning electron microscopy (SEM), and X-ray diffraction (XRD) in detail. The vapor−solid (VS) growth mechanism was proposed to

DOI: 10.1021/acsami.8b11676
ACS Appl. Mater. Interfaces 2018, 10, 35477−35486

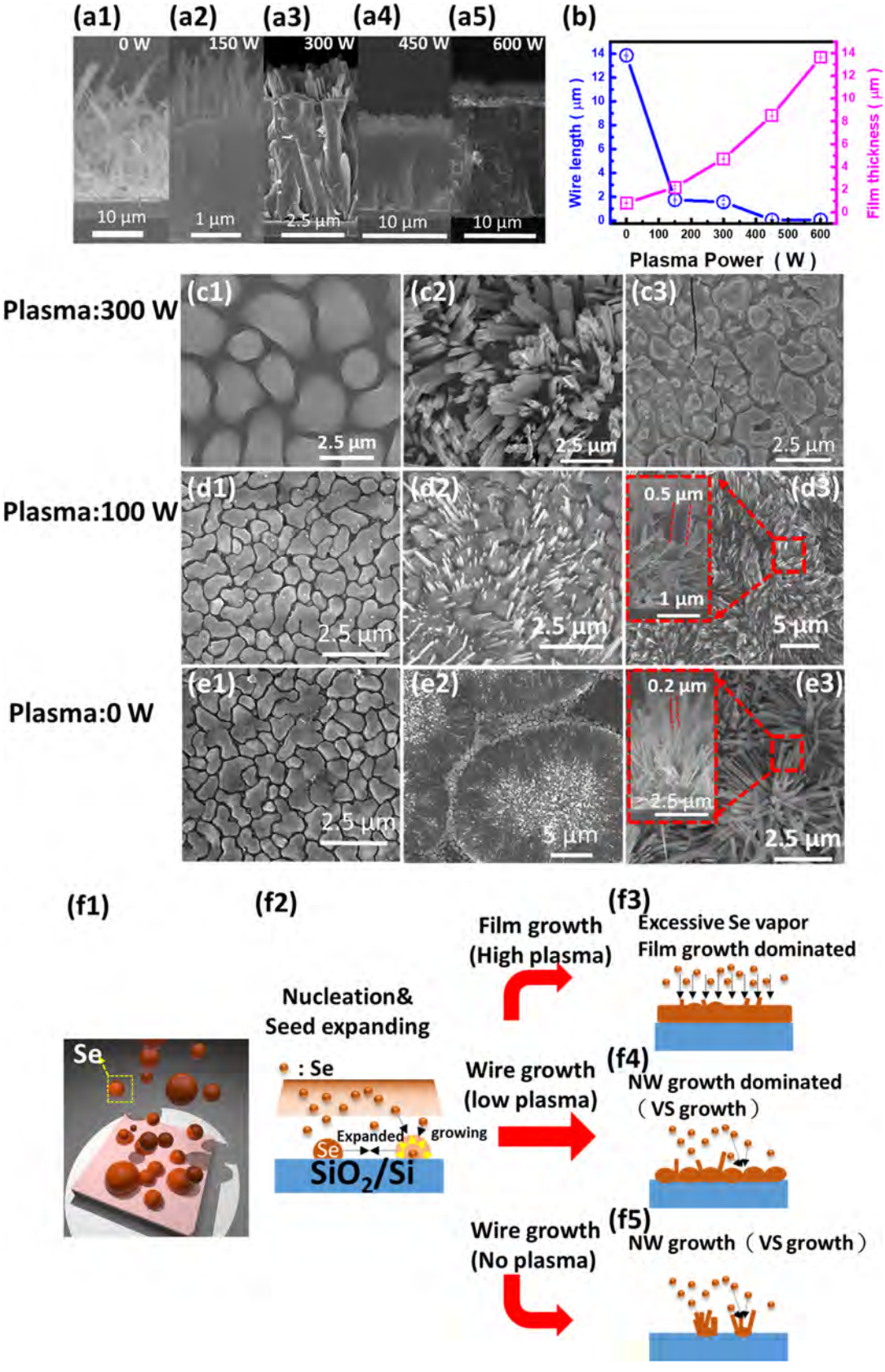

Figure 2. (a1−a5) SEM images of Se nanostructures from NWs to thin films at different plasma powers. (b) Plots of wire length and film thickness as the function of plasma powers. Morphologies of Se nanostructures varied with with plasma powers of (c1−c3) 300 W, (d1−d3) 100 W, and (e1−e3) 0 W. (f1−f5) Schematics of the growth mechanism for Se nanostructures under various plasma powers.

DOI: 10.1021/acsami.8b11676
ACS Appl. Mater. Interfaces 2018, 10, 35477−35486

elucidate the process of Se NWs arrays/thin film growth. An In layer as an inserting layer was discovered to enhance the adhesion behavior between Se nanostructures and substrates, where the enhanced adhesive force was measured up to 4 MPa, a 50% improvement compared with that without the In layer. The enhanced adhesion behavior can be explained by the mechanical interlocking and the interface alloying between Se and In. Furthermore, the growth conditions of nanowires arrays to the thin film were optimized by measuring the best performance as photodetectors. The broad photoresponse covering detecting ranges from near UV (405 nm) to IR (1550 nm) with excellent photoresponse time less than 25 ms and responsivity of 6 mA W^{-1} can be achieved. To the best of our understanding, this is the first report of photodetecting toward the IR wavelength range using 1D/2D Se/In_2Se_3 heterostructure as the sensing component.

RESULTS AND CONCLUSIONS

Figure 1a illustrates the configuration of the plasma-assisted selenization furnace, consisting of Se tank, radio frequency coils, and heating stage. When the temperature in the Se tank exceeds the vaporization point of the Se source at 300 °C, the Se vapors will be generated and flow downward through the plasma coil, resulting in the formation of ionized Se and then get deposited on In/SiO_2/Si substrates at the low substrate temperature of 100 °C. The crystallinity of the as-grown film was examined by Raman and XRD. Figure 1b shows the XRD results of samples through the plasma-assisted selenization process. The detected peaks at 2θ of 29.74, 43.72, 45.44, 51.8, 55.96, and 61.5° correspond to the (101), (101), (102), (111), (201), (003), and (103) planes were indexed to a trigonal phase, which are in prefect agreement with the published values.[23,24] Also, the peak located at 32.96° is attributed to the Indium (In)(101) plane and the importance of the In insertion layer to enhance adhesion between 1D or 2D Se nanostructures and substrates will be addressed in the following section.[25] From the result of the Raman spectrum as shown in Figure 1c, the strong Raman peak located at 235 cm^{-1} is a characteristic stretching mode of a helical chain-like structure, namely, A1 mode, which only exists in a representative feature of the trigonal phase,[16] whereas the peak located at 143 cm^{-1} corresponds to the transverse optical phonon mode, namely, E mode.[26] The morphologies of Se nanostructures were investigated by scanning electron microscopy (SEM) and transmission electron microscopy (TEM). A typical SEM image is shown in Figure 1d1, which confirms the high density of the Se NWs arrays. To reveal the crystallinity of the Se NWs arrays, Se NWs were scratched from the substrate into an alcohol solution and then drop-casted on Cu grids for microstructure analysis. Figure 1d2 shows a representative TEM image. The atomic high-resolution TEM image as shown in the upper inset of Figure 1d2 distinctly displays the single-crystalline feature of the Se NW. The selected area electron diffraction result also reveals the preferential growth direction of the Se NW along [001], which is perpendicular to the (001) plane with an internal spacing of 0.502 nm. In addition, another internal spacing of 0.351 nm corresponding to the $(1\bar{1}0)$ plane was indexed.

An interesting feature of controllability in the morphologies of Se nanostructures from 1D NWs arrays to 2D thin film by the plasma-assisted physical vapor deposition relies on different plasma powers at the fixed substrate temperature of 100 °C and deposition time of 90 min as well as the identical Se tank temperature of 300 °C as shown in Figure 2a1−a5. The NWs arrays can be achieved without the plasma environment, whereas the growth of the thin film starts once the plasma power increases. Furthermore, Figure 2b shows the plots of the wire length and the film thickness as the function of plasma powers from Se 1D NWs arrays to Se 2D thin films. Obviously, the growth of nanowires dominates the entire growth process as the plasma power is <200 W. When the plasma power exceeds 200 W, the lateral growth dominates the entire growth process, resulting in the growth of thin film rather than the NWs arrays. Two possible mechanisms, vapor−solid growth mechanism (VS)[27,28] and catalytic vapor−liquid−solid (VLS) mechanisms,[29] have been proposed to elucidate the entire growth mechanism of the 1D nanowires. No catalyst on the top of nanowires, as confirmed by the TEM image shown in Figure 1d2, indicates that the VLS mechanism in our cases can be ruled out and the vapor−solid (VS) growth mechanism may be the possible growth mechanism of Se NWs mostly in a template-free vapor transport situation because of an anisotropic surface energy.[30,31] Basically, the VS growth mechanism can be explained by a well-known two-dimensional (2D) nucleation probability, which highly relies on different surface free energies at different planes.[32] To shed light on this part, the growth of the Se 1D nanowires into 2D thin films at different stages were confirmed at different times with the plasma power of 300 W as shown in Figure 2c1−c3 and with the plasma power of 100 W as shown in Figure 2d1−d3, as well as without the plasma environment (Figure 2e1−e3). Figure 2f1−f5 schematically illustrates the exact dynamic growth mechanisms of the Se nanostructures from 1D NWs arrays to the 2D thin film. In an initial stage, the formation of coherent three-dimensional (3D) islands is preferred rather than the smooth film growth, allowing a significant reduction of total energy due to the laterally elastic relaxation of 3D islands against coarsening (Ostwald ripening) via Volmer−Weber growth.[33] Therefore, Se seeds nucleate (Figure 2c1,d1,e1,f1), followed by the expansion of seeds by merging nearby seeds into large one (Figure 2f2). Subsequently, the newly arriving Se clusters/atoms are preferably and epitaxially formed on these as-grown Se 3D nuclei owing to the reduction of surface free energy, resulting in the formation of Se NWs arrays along the [001] direction via the vapor−solid (VS) growth, which restricts the lateral growth as shown in Figure 2e2,e3,f5 because (001) has the lowest surface energy. The results are also consistent with the NW growth direction of [001] observed by the TEM image (Figure 1d2). Note that the structural defects on top of Se nuclei, such as stacking faults and microtwins may also accelerate the 1D NW growth.[34] Once the plasma function was applied, Se atoms will be ionized into Se radicals with a high chemical activity, resulting in the specific surface free energy of Se vacuum (γ_s) being larger than that In/SiO_2 substrate Se film (γ_i) + Se film vacuum (γ), where Frank-van der Merwe growth, namely, a layer-by-layer growth, dominates the entire growth.[35] As a result, the lateral adatom diffusion of Se clusters, namely, the lateral overcoating along the side wall of Se NWs occurs as well, leading to the larger diameter of Se NWs, whereas a Se thin film is formed at the bottom as shown in Figure 2d3,f4. Note that different plasma power may lead to Se radicals with different chemical activities. The higher the plasma power, the higher the chemical activity of Se radical. This is why we can see the Se NWs arrays grow on top of the 2D Se thin film at the plasma power below 300 W. However, when the plasma

DOI: 10.1021/acsami.8b11676
ACS Appl. Mater. Interfaces 2018, 10, 35477−35486

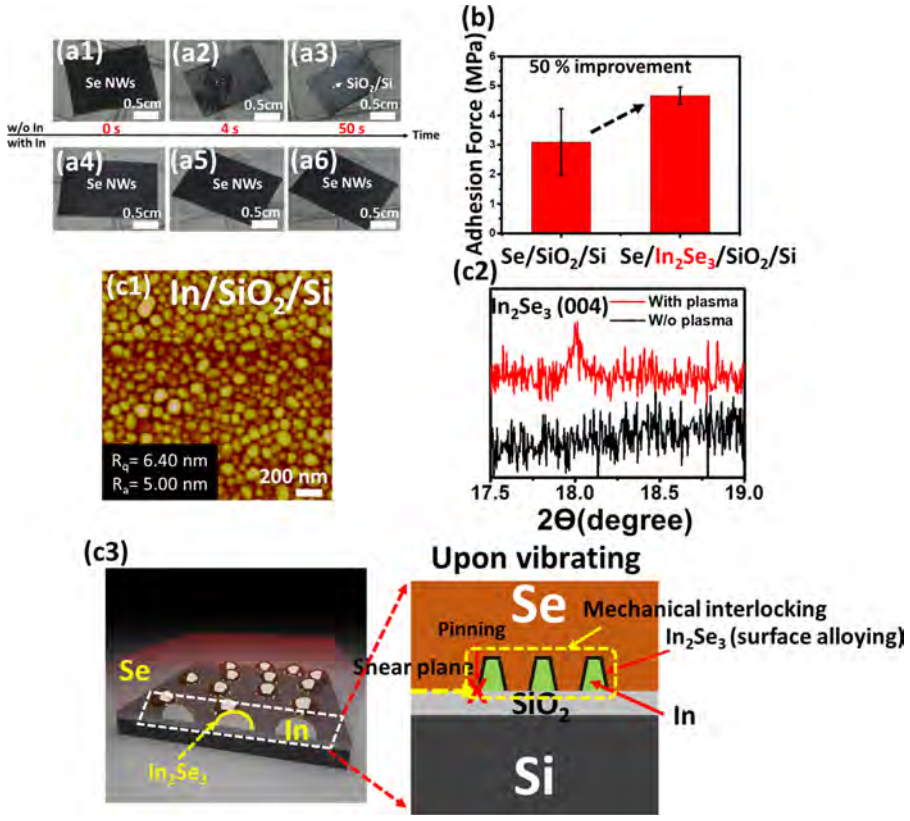

Figure 3. Screenshots of devices with (a1)−(a3) and without (a4)−(a6) the In as the inserted layers through the process of ultrasonic vibration. (b) Adhesive force measurements of Se nanostructures with In and without In as inserted layers. (c1) An AFM image of the In layer deposited as a result of the island-like surface. (c2) XRD spectra of Se/In/SiO_2/Si with and without the plasma treatment. (c3) Schematics of Se/In/SiO_2/Si through the vibrating test, demonstrating the resistance of shear stress by interlocking and alloying. Upon vibrating, the dynamic shear stress generated along the shear plane of Se/SiO_2/Si, as a result of detachmewent of Se from the substrate.

power is >300 W, Se radicals with high chemical activity prefers the Se radicals to assemble into a thin film rather than growth of NWs as shown in Figure 2c3,d3.

For a well-performed sensor, the stability of devices' performance is a critical issue whenever the devices are operated in static or dynamic status.[36] The importance of the In layer as the insertion layer between Se NWs/films and SiO_2/Si substrate for the great enhancement of the adhesion upon a vibrating condition was investigated. In addition, the deposition of Se nanostructures without the In insertion layer was prepared as the reference for the comparison. Note that the growth of Se NWs can still be achieved on the substrate without the In insertion layer (Figure S1), confirming there is no influence of the In insertion layer on the growth of Se nanostructures. The corresponding videos of the two samples under the mechanical sonication process are shown in the Supporting Information (Videos S1 and S2 represent the growth of Se nanowires with and without the In insertion layer, respectively). A series optical images taken from Video S1 are shown in Figure 3a1−a3 without the In insertion layer on SiO_2/Si substrates during a high-frequency sonication process as the examination of mechanical stability by time. Clearly, the Se films peeled off within 4 s due to the poor adhesion on the substrate. Interestingly, after adding the In insertion layer, the Se 1D NWs arrays or 2D thin film were firmly adhered to the substrate against the high-frequency sonication as shown in Figure 3a4−a6 taken from Video S2. Furthermore, the adhesive force of Se/SiO_2/Si and Se/In/SiO_2/Si by the pull-off test was quantitatively measured as shown in Figure 3b. Obviously, the adhesive force can be up to ∼4 MPa, which is a 50% enhancement in identical growth condition without the addition of the In insertion layer. The key to the enhanced adhesion by the In insertion layer is the two possible mechanisms, including mechanical interlocking and surface alloying behaviors.[37−39] The distribution and morphology of In layer deposited by sputtering on SiO_2/Si were revealed by atomic force microscopy (AFM), as shown in Figure 3c1, confirming the island-like clusters because of the large surface energy when touching with the SiO_2/Si substrate. In addition to the adding of the In layer, we also found that In_2O_3 and Sn layers have identical morphologies, resulting in the enhancement of the adhesion behavior as shown in Figure S2a,b. For comparison, the SiO_2 or the SnO_2 layer, as shown in Figure S2c,d, is not able to against the shear plane slipping because of the smooth surface. In addition to the enhanced adhesion by mechanical interlocking, the surface alloying due to the formation of the In_2Se_3 phase confirmed by temporal coherent XRD spectrum at the interface between the In insertion layer and the Se 1D NWs arrays or the 2D thin films is another reason to enhance the adhesion force as shown in Figure 3c2, where a peak located at ∼18° related to the In_2Se_3(004) plane was observed. TEM and HRTEM images between the Se NWs arrays and the SiO_2 layer confirm the existence of In_2Se_3, as shown in Figure S3a,b, where two internal spacings of 0.293 and 0.65 nm corresponding to (022) and (004) were confirmed and a diffraction pattern by fast Fourier transformation was also indexed with the zone axis of [001]. The mechanism of the enhanced adhesion behavior can be

DOI: 10.1021/acsami.8b11676
ACS Appl. Mater. Interfaces 2018, 10, 35477−35486

explained by the island-like In clusters acting as a locker, which is the so-called mechanical interlocking associated with the formation of the In_2Se_3 phase through the surface alloying behavior, yielding the strong bond with Se 1D/2D nanostructures against the shear plane slipping as shown in Figure 3c3.

To investigate the optoelectrical performance of photodetectors using Se 1D/2D nanostructures on the SiO_2/Si substrate with the In insertion layer, the fingerprint-type electrodes were prepared by a hard mask using Cr/Au as the electrode deposited by the E-beam and the photoresponse properties were recorded under monochromatic light illumination at a constant bias voltage. Note that the metal electrode plays an important role of collecting the photocurrent. However, metal itself would reflect the incident light, resulting in the loss of photon. Hence, the finger-shaped electrode was designed by referring the interdigital configuration, which was commonly used in solar cell and applied to the photodetector for highly efficient current collection and maximizing the photon flux in the sample. Obviously, linear $I-V$ curves recorded from all the devices reveal Ohmic contacts regardless of different plasma powers, as shown in Figure S4.[40] Furthermore, the suppression of dark current was a critical parameter for evaluating the performances of photodevices when operating devices at extremely low intensity of light.[41,42] Hence, the on/off ratio and the dark current were recorded for the Se 1D NWs arrays/2D thin films photodetectors where a bias voltage of 0.5 V was applied. Note that the on/off current ratio is defined as the ratio of the on current to the dark current, namely, I_{on}/I_{dark}. To shed light on the best performance of the Se 1D NWs arrays/2D thin films as photodetectors, the on/off current ratios and the dark current at different plasma powers were measured as shown in Figure S5a, where the corresponding on/off current ratios of 10.1, 122.8, 695.8, 233.6, and 41.1 under plasma powers of 0, 150, 300, 450, and 600 W are plotted, respectively. The decrease in the dark current can be found as the plasma power increases from 150 to 300 W, whereas the dark current increases as the plasma power increases from 300 to 600 W. We expect that the increase in the dark current can be attributed the increase in the leakage current. To further shed light on this topic, Figure S5b plots the wire width as the function of plasma powers. In the plasma power below 300 W, the dominated growth of Se 1D NWs arrays can lead to the higher resistance because of the longer nanowire morphology, resulting in less leakage current with the lower dark current. As the structure changes from NWs arrays into thin films, the chance of the leakage current through the grain boundary increases as the plasma power increases, leading to the increase in dark current. Consequently, the Se hybrid nanostructure consisting of 1D Se NWs arrays on the top of 2D Se thin film at the optimal plasma power of 300 W has the lowest dark current with the highest on/off ratio of ~700. Furthermore, photoresponsivity (R_λ), defined as $R_\lambda = I_{rise}/PS$, is an important factor for estimating the performance of photodetectors, where P is the laser intensity applied on the samples and S is defined as the illuminated areas of samples. By substituting the corresponding values into this equation, R_λ of 6 mA W^{-m} can be calculated. Figure S5c displays the $I-V$ curve upon the illumination of 638 nm laser with different altering powers. The linear dependence of current and applied voltage demonstrates the Ohmic contact under different light intensities. A time-resolved switching photocurrent at 0.5 V with different laser wavelengths of 405, 514, and 638 nm at the light intensity of 0.3 mW mm^{-2} was conducted and the corresponding results are shown in Figure 4a. Once the laser is turned on, the current abruptly increases

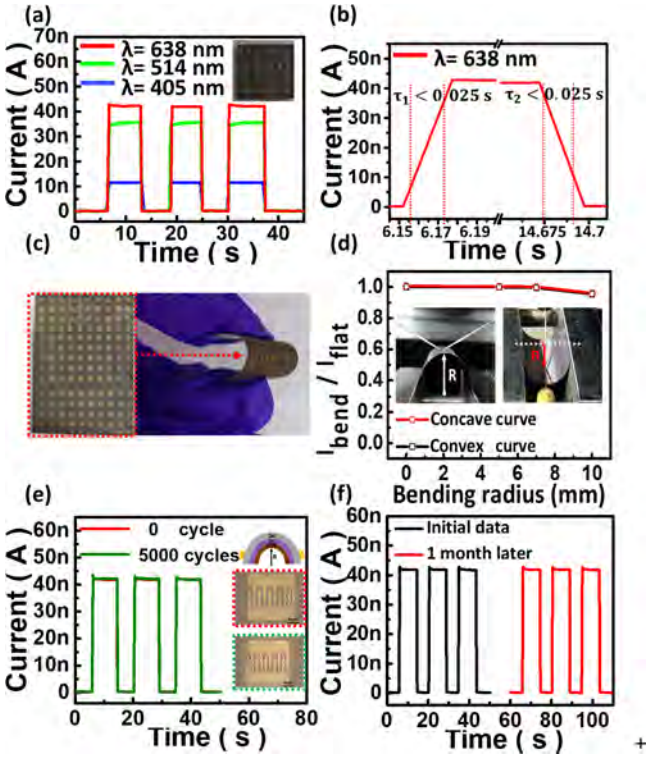

Figure 4. (a) Results of $I-t$ sweep of Se photodetectors illuminated by 638, 514, and 405 nm wavelengths with the identical light intensity at 0.3 mW mm^{-2} and a bias voltage of 0.5 V. (b) Fitting results of the rise time and the decay time of Se photodetectors. (c) An optical image of the fabricated Se/In photodetector upon the bending tests. (d) The ratio of photocurrent recorded upon the bending with different bending radii over that recorded in a flat status. The inset shows photos of the Se/In photodetector in the concave and convex state. (e) Mechanical endurance test of photodetectors by $I-t$ measurement before and after 5000 cycles. Inset proves the integrity of devices after 5000 cycling bending test. (f) Stability test of Se/In photodetectors by $I-t$ measurements over 1 month.

into the saturated photocurrent and immediately returns to the initial value when the excited laser is turn off. The wavelength dependence of $I-V$ curve of Se 1D/2D photodetectors are shown in Figure S6, revealing that the current linearly increases with increasing voltage, confirming the Ohmic contact between Cr/Au and Se 1D/2D. The square-waveform results indicate the outstanding performance of our Se photodetectors. Not only response to the laser wavelength of 638 nm, but also 514 and 405 nm excited wavelengths are able to trigger the process of generating electron–hole pairs as well, demonstrating the broad-ranged photoresponses. The trend of the decrease in current with short-wavelength laser is possibly due to the formation of the significant Auger recombination process.[43] The photons with shorter wavelength easily trigger the inner-shell electron–hole pairs and thus the formation of Auger electrons, resulting in the release of energy.[43] Figure 4b depicts the single current characteristic of the device measured at the identical illumination condition (the excited laser at a wavelength of 638 nm with the applied bias of 0.5 V and the light intensity of 0.3 mW mm^{-2}). The rise time is defined as

DOI: 10.1021/acsami.8b11676
ACS Appl. Mater. Interfaces 2018, 10, 35477–35486

the time taken for the intensity of the photocurrent to increase from 10 to 90% and the decay time is defined as the time interval for the decrease in current from 90 to 10%. As a result, the rise and decay times can be found to be less than 0.25 s.

Furthermore, it is well known that flexible electronics directly built on flexible substrates have created more intensive interest, such as sensors,[44] thin-film solar cells,[45,46] artificial skins,[47−49] and light-emitting diodes. The growth of Se 1D and 2D nanostructures by plasma-assisted growth occurs in an extremely low temperature, which can be down to 100 °C and applied on plastic substrates as flexible photodetectors. To demonstrate this part, the best performance as the photodetector using Se hybrid nanostructures (Se 1D NWs arrays on the 2D Se thin film) was grown at the plasma power of 300 on a poly(ethylene terephthalate) (PET) substrate, followed by the device fabrication based on the fingerprint configuration as shown in Figure 4c. To understand stability and durability of the devices under compressive and tensile stress, Se hybrid nanostructures-based devices were concaved and convexed with different bending radii repeatedly. Note that the ratios of I_{bend}/I_{flat} are used to shed light on the reliability. Figure 4d shows the corresponding ratios of I_{bend}/I_{flat} calculated at varied bending radii of 5, 7, and 10 mm at the excited wavelength of 632 nm. Remarkably, regardless of the different bending radii applied, the ratio of I_{bend}/I_{flat} is nearly close to 1, implying the great tolerance of deformation. To examine their durability, the Se hybrid nanostructure-based devices were subject to cyclic testes. Figure 4e shows the $I-t$ measurements after 5000 bending cycles. Obviously, no degradation of performance was observed, demonstrating the rugged reliability of the Se hybrid nanostructures-based photodetectors. The insets show the OM images after 5000 bending cycles, proving the fascinating integrity through the cyclic bending tests. In addition, the Se hybrid nanostructures-based photodetectors were exposed fully in air over 1 month followed by the $I-t$ measurements. Interestingly, the performance still remains the same as that of pristine, as shown in Figure 4f.

The cost-effective and efficient IR photodetection at room temperature is still a technological challenge due to the lack of appropriate active photosensing materials. Here, for the first time, we demonstrate the photoresponse of Se hybrid nanostructures-based photodetectors on the SiO_2/Si substrate in the infrared range where a laser with a wavelength of 1550 nm was chosen as a light source. The time-dependent current measurements of the devices were conducted and the laser on/off mode were manipulated by a mechanical chopper with a frequency of 0.2 Hz. The reproducible on and off states of photodetectors by each cycle at different laser power from dark to 0.65 mW mm^{-2} are presented in Figure 5a, indicating excellent periodicity and stability. The corresponding $I-V$ characteristics as the function of power density from dark to 0.65 mW mm^{-2} are shown in Figure S7. At the same bias, the current increases as the power density increases, proving the sensitivity to infrared light. As a result, the ratio of the on/off current of up to 5 with a low driving voltage of ∼0.5 V with a photoresponsivity of 9×10^{-3} mA W^{-1}, exhibiting an ideal infrared photodetector with the lower power consumption. The $\tau 1$ and $\tau 2$ of 0.11 and 0.11 s were also extracted out, respectively as shown in Figure 5b and is comparable with other reported results.[50−52] Furthermore, the performance of Se hybrid nanostructure-based devices on the flexible substrate was also demonstrated as shown in Figure 5c,d. Inset in Figure 5d shows the photograph of a flexible device during the bending tests, for which the bending radius (R) is the distance from the flat state to the top during the bending process. Figure 5c shows the results of the $I-t$ measurements as a function of varied bending radii, confirming a distinct and prompt reaction upon the illumination regardless of different bending radii. The repeatable $I-t$ curves proved the performance stability on the flexible substrate. Note that the photocurrent is little lesser than that recorded on the rigid substrate, which is possibly attributed to the slight detachment of the electrode out of the substrate, and gradually decreases as curve of the device increases. Figure 5d plots the ratio of I_{bend}/I_{flat} as the function of bending radii. Obviously, on current decreased linearly as the bending radius increased with the decay rate of 0.1/1 mm^{-1}. The possible mechanism for the high photosensitivity of Se hybrid nanostructure-based photodetectors to IR can be explained by the existence of defect levels in the amorphous region with different termination attached to different molecules such as H^-, OH^-, and O^-, resulting in the defect energy levels of 0.5−0.9 eV below the conduction band.[11,53] In addition, the optical absorption of Se in the ranges of 400−1600 nm was measured, confirming the possibility of absorption in the long-wavelength range (Figure S8). Table 1 compares the photoelectricity results of different Se nanostructure-based photodetectors with previous reports from the literature. Obviously, Se hybrid nanostructure-based photodetectors exhibit comparable performance in terms of responsivity and low power consumption, especially the wide-range photoresponse from UV to IR. Based on the above results, our Se hybrid nanostructure-based photodetector offers extreme flexibility, good bending endurance, high electrical stability, and air stability, demonstrating the great potential toward the real-world wearable optoelectronic applications.

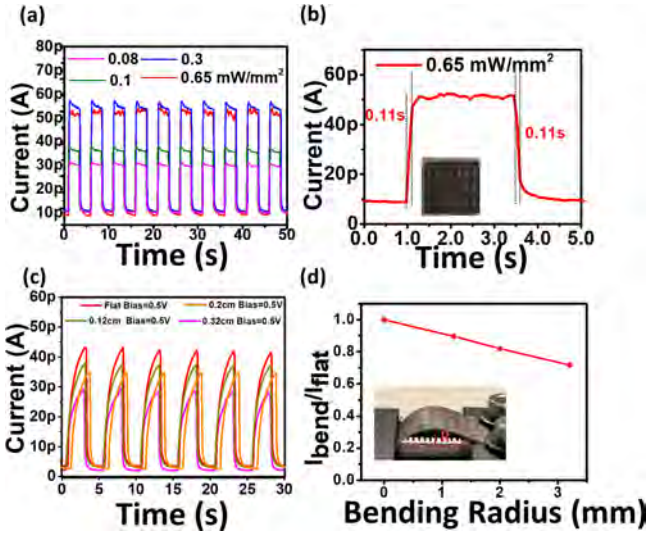

Figure 5. (a) Photodetection performance upon 1550 nm illumination on a rigid substrate. (b) High time-resolution measurement. The chopped frequency is 0.2 Hz, the bias voltage is 0.5 V. (c) Results of $I-t$ measurements as the function of varied bending radii. (d) Mechanical stability test of devices upon 1550 nm illumination on flexible substrates with different bending radii. The inset shows the image of devices upon bending and the definition of the radius.

CONCLUSIONS

In summary, a low-temperature and catalyst-free approach to synthesize Se 1D NWs arrays and 2D thin film structures by

DOI: 10.1021/acsami.8b11676
ACS Appl. Mater. Interfaces 2018, 10, 35477−35486

Table 1. Comparison of the Performances of the Other Se Photodetectors[a]

process time/temp. (h °C^{-1})	measurement condition	on/off ratio	τ_{on} (ms)	τ_{off} (ms)	R (mA W^{-1})	substrate	
50/—	514 nm V_{bias} = 0.1 V	0.6	—	—	—	rigid	13
1/250	638 nm V_{bias} = 3 V	430	—	—	3.27 × 10^{7} 759	flexible	14
13/150	610 nm V_{bias} = 5 V	32	0.32	23	19 1280	rigid	15
1.5/100	638 nm V_{bias} = 0.5 V	700	<25	<25	6	flexible	this work
1.5/100	514 nm V_{bias} = 0.5 V	583.3	<25	<25	4	flexible	this work
1.5/100	405 nm V_{bias} = 0.5 V	191.6	<25	<25	0.4	flexible	this work
1.5/100	1550 nm V_{bias} = 0.5 V	5	<110	<110	9 × 10^{-3}	flexible	this work

[a]"—": not mentioned in the reference.

the plasma-assisted selenization process was demonstrated. Contrary to the other proposed methods, the plasma-assisted selenization process enables time-saving and environmentally friendly approach for preparing low-dimensional Se structures as well as avoiding pollution problem and poor electric characteristic. Moreover, by adjusting the plasma power, the appearance of Se could to be controlled from nanowires to film. By depositing the In layer before Se 1D NWs arrays and 2D thin films, the adhesion between Se 1D and 2D nanostructures can be greatly improved, such that the enhanced adhesive force of 50% improvement can be confirmed by pulling-off tests. Through XRD and AFM results, detailed investigation of interfaces was conducted, confirming the enhanced adhesion ability attributed to the mechanism of interlocking by In islands and alloying effect by forming In_2Se_3 alloy on In islands. Se hybrid nanostructures photodetectors exhibiting a distinct on/off ratio up to 700 with responsivity of 6 mA W^{-1} and fast responses in 25 ms were fabricated. Flexible Se hybrid nanostructure-based photodetectors exhibit a wide spectrum of photoresponses from UV to IR ranges, with outstanding mechanical flexibility over 5000 cycles bending test and air durability over 1 month, proving that they are potential candidates in wearable optoelectronic applications.

METHODS

Growth of Se 1D and 2D Nanostructures by Plasma-Assisted Selenization Process. First, a 30 nm thick In layer was deposited on SiO_2 (50 nm)/Si (300 nm) substrates by sputtering at the flow rate of 250 sccm N_2. Subsequently, the sample was placed into the substrate holder in the furnace chamber followed by the growth of Se 1D and 2D nanostructures by the plasma-assisted selenization process. During the plasma-assisted selenization process, the SiO_2 (50 nm)/Si (300 nm) substrates were slowly ramped to 100 °C in 30 min and was maintained at 100 °C for 60 min with various plasma powers from 0, 150, 300, 450, and 600 W at fixed gas ambient of hydrogen (H_2) and nitrogen (N_2) flows of 80 and 40 sccm with the fixed pressure of 2.5 torr. After 90 min, the chamber was cooled down to room temperature at a nitrogen (N_2) gas flow of 200 sccm.

Fabrication Processes and Measurements of Photodetectors. The photoresponse characteristics of Se NWs photodetectors were thoroughly measured at room temperature. For the fabrication of devices, finger-shaped electrodes were defined by the hard mask and followed by the deposition of Cr/Au with 5:50 nm deposited by electron gun evaporation system on SiO_2/Si substrates. Owing to the low processing temperature, the deposition of Se on PET substrates was demonstrated as well. The photoresponse of Se NWs photodetectors on SiO_2/Si and PET were recorded, respectively, by Keithley 4200 upon illumination of the laser with 632, 514, and 405 nm wavelengths.

Characterizations. Surface morphologies of the samples were observed by field-emission scanning electron microscope (Hitachi, SU8010). Crystal structure and sample quality were verified by Raman spectroscopy (HORIBA Jobin-Yvon, LabRAM, HR800) equipped with 532 nm laser and X-ray diffraction (Shimadzu XRD-6000, Cu Kα, λ = 0.154 nm) scanning from 15 to 65°. The lattice spacing of the samples was analyzed by a high-resolution transmission electron microscope (HRTEM; JEM-3000F FEGTEM, JEOL, Japan) operated at 300 kV.

Adhesive Force Measurements. The adhesive strength measurements of Se NWs and SiO_2/Si substrate and Se NWs/In/SiO_2/Si substrate were conducted by the pull-off method. At the beginning, the aluminum stud was coated with epoxy to stick to the surface of samples and followed by curing for 6 h at 50 °C. Once dried, the testing process was executed by using a pull-off tester (PosiTest AT-M, DeFelsco) in accordance with ASTM D4541/D7234.

ASSOCIATED CONTENT

Supporting Information

The Supporting Information is available free of charge on the ACS Publications website at DOI: 10.1021/acsami.8b11676.

SEM image of Se NWs synthesized on a SiO_2/Si substrate (Figure S1); AFM results of surface morphology (Figure S2); low magnification TEM image of the interfaces between the Se and the In (Figure S3); I–V curves of Se 1D NWs photodetectors (Figure S4) (PDF)

Growth of Se nanowires with and without the In insertion layer (Videos S1 and S2) (AVI) (AVI)

AUTHOR INFORMATION

Corresponding Authors

*E-mail: chshen@narlabs.org.tw (C.-H.S.).
*E-mail: ylchueh@mx.nthu.edu.tw (Y.-L.C.).

ORCID

Tzu-Chien Wei: 0000-0002-9608-8275
Johnny C. Ho: 0000-0003-3000-8794
Kung-Hwa Wei: 0000-0002-0248-4091
Yu-Lun Chueh: 0000-0002-0155-9987

Author Contributions

○Y.-Z.C. and Y.-T.Y. contributed equally to this work.

DOI: 10.1021/acsami.8b11676
ACS Appl. Mater. Interfaces 2018, 10, 35477−35486

Notes

The authors declare no competing financial interest.

■ ACKNOWLEDGMENTS

The research is supported by Ministry of Science and Technology through Grant through grants nos. 107-2923-E-007-002-MY3, 107-2112-M-007-030-MY3, 106-2923-E-007-006-MY2, 105-2119-M-009-009, and 107-3017-F-007-002, 107-3017-F-009-003 and the National Tsing Hua University through Grant no. 106N509CE1. Y.-L.C. greatly appreciates the use of the facility at CNMM.

■ REFERENCES

(1) Medina, H.; Li, J.-G.; Su, T.-Y.; Lan, Y.-W.; Lee, S.-H.; Chen, C.-W.; Chen, Y.-Z.; Manikandan, A.; Tsai, S.-H.; Navabi, A.; Zhu, X.; Shih, Y.-C.; Lin, W.-S.; Yang, J.-H.; Thomas, S. R.; Wu, B.-W.; Shen, C.-H.; Shieh, J.-M.; Lin, H.-N.; Javey, A.; Wang, K. L.; Chueh, Y.-L. Wafer-Scale Growth of WSe_2 Monolayers Toward Phase-Engineered Hybrid WOx/WSe2 Films with Sub-ppb NOx Gas Sensing by a Low-Temperature Plasma-Assisted Selenization Process. *Chem. Mater.* **2017**, *29*, 1587−1598.

(2) Guo, H.; Lan, C.; Zhou, Z.; Sun, P.; Wei, D.; Li, C. Transparent, Flexible, and Stretchable WS_2 Based Humidity Sensors for Electronic Skin. *Nanoscale* **2017**, *9*, 6246−6253.

(3) Trung, T. Q.; Ramasundaram, S.; Hwang, B. U.; Lee, N. E. An All-Elastomeric Transparent and Stretchable Temperature Sensor for Body-Attachable Wearable Electronics. *Adv. Mater.* **2016**, *28*, 502−509.

(4) Chen, Y.-Z.; Medina, H.; Wang, S.-W.; Su, T.-Y.; Li, J.-G.; Yen, W.-C.; Cheng, K.-Y.; Kuo, H.-C.; Shen, G.; Chueh, Y.-L. Low-Temperature and Ultrafast Synthesis of Patternable Few-Layer Transition Metal Dichacogenides with Controllable Stacking Alignment by a Microwave-Assisted Selenization Process. *Chem. Mater.* **2016**, *28*, 1147−1154.

(5) Williams, K. J.; Nichols, L. T.; Esman, R. D. Photodetector Nonlinearity Limitations on a High-Dynamic Range 3 GHz Fiber Optic Link. *J. Lightwave Technol.* **1998**, *16*, 192−199.

(6) Zheng, Z.; Gan, L.; Li, H.; Ma, Y.; Bando, Y.; Golberg, D.; Zhai, T. A Fully Transparent and Flexible Ultraviolet−Visible Photodetector Based on Controlled Electrospun ZnO-CdO Heterojunction Nanofiber Arrays. *Adv. Funct. Mater.* **2015**, *25*, 5885−5894.

(7) Ma, Y.; Qi, L.; Ma, J.; Cheng, H. Micelle-Mediated Synthesis of Single-Crystalline Selenium Nanotubes. *Adv. Mater.* **2004**, *16*, 1023−1026.

(8) Smith, W. Effect of Light on Selenium during the Passage of an Electrical Current. *Nature* **1873**, *7*, No. 303.

(9) Mertz, W. The Essential Trace Elements. *Science* **1981**, *213*, 1332−1338.

(10) Hu, K.; Chen, H.; Jiang, M.; Teng, F.; Zheng, L.; Fang, X. Broadband Photoresponse Enhancement of a High-Performance t-Se Microtube Photodetector by Plasmonic Metallic Nanoparticles. *Adv. Funct. Mater.* **2016**, *26*, 6641−6648.

(11) Luo, L.-B.; Yang, X.-B.; Liang, F.-X.; Jie, J.-S.; Li, Q.; Zhu, Z.-F.; Wu, C.-Y.; Yu, Y.-Q.; Wang, L. Transparent and Flexible Selenium Nanobelt-based Visible Light Photodetector. *CrystEngComm* **2012**, *14*, 1942−1947.

(12) Liao, Z.-M.; Hou, C.; Liu, L.-P.; Yu, D.-P. Temperature Dependence of Photoelectrical Properties of Single Selenium Nanowires. *Nanoscale Res. Lett.* **2010**, *5*, 926−929.

(13) Chen, H.; Shin, D.-W.; Nam, J.-G.; Kwon, K.-W.; Yoo, J.-B. Selenium Nanowires and Nanotubes Synthesized via a Facile Template-free Solution Method. *Mater. Res. Bull.* **2010**, *45*, 699−704.

(14) Peng, L.; Yurong, M.; Weiwei, C.; Zhenzhong, W.; Jian, W.; Limin, Q.; Dongmin, C. Photoconductivity of Single-crystalline Selenium Nanotubes. *Nanotechnology* **2007**, *18*, No. 205704.

(15) Cheng, B.; Samulski, E. T. Rapid, High yield, Solution-mediated Transformation of Polycrystalline Selenium Powder into Single-crystal Nanowires. *Chem. Commun.* **2003**, 2024−2025.

(16) Li, X.; Li, Y.; Li, S.; Zhou, W.; Chu, H.; Chen, W.; Li, I. L.; Tang, Z. Single Crystalline Trigonal Selenium Nanotubes and Nanowires Synthesized by Sonochemical Process. *Cryst. Growth Des.* **2005**, *5*, 911−916.

(17) Lu, Q.; Gao, F.; Komarneni, S. Cellulose-Directed Growth of Selenium Nanobelts in Solution. *Chem. Mater.* **2006**, *18*, 159−163.

(18) Zhang, B.; Dai, W.; Ye, X.; Zuo, F.; Xie, Y. Photothermally Assisted Solution-Phase Synthesis of Microscale Tubes, Rods, Shuttles, and an Urchin-Like Assembly of Single-Crystalline Trigonal Selenium. *Angew. Chem., Int. Ed.* **2006**, *45*, 2571−2574.

(19) Ozin, G. A. Nanochemistry: Synthesis in Diminishing Dimensions. *Adv. Mater.* **1992**, *4*, 612−649.

(20) Fendler, J. H. Atomic and Molecular Clusters in Membrane Mimetic Chemistry. *Chem. Rev.* **1987**, *87*, 877−899.

(21) Luo, L. B.; Jie, J. S.; Chen, Z. H.; Zhang, X. J.; Fan, X.; Yuan, G. D.; He, Z. B.; Zhang, W. F.; Zhang, W. J.; Lee, S. T. Photoconductive Properties of Selenium Nanowire Photodetectors. *J. Nanosci. Nanotechnol.* **2009**, *9*, 6292−6298.

(22) Xie, Q.; Dai, Z.; Huang, W.; Zhang, W.; Ma, D.; Hu, X.; Qian, Y. Large-Scale Synthesis and Growth Mechanism of Single-Crystal Se Nanobelts. *Cryst. Growth Des.* **2006**, *6*, 1514−1517.

(23) Chen, M.; Gao, L. Selenium Nanotube Synthesized via a Facile Template-free Hydrothermal Method. *Chem. Phys. Lett.* **2006**, *417*, 132−136.

(24) Zhang, H.; Zuo, M.; Tan, S.; Li, G.; Zhang, S.; Hou, J. Carbothermal Chemical Vapor Deposition Route to Se One-Dimensional Nanostructures and Their Optical Properties. *J. Phys. Chem. B* **2005**, *109*, 10653−10657.

(25) Kim, J.; Schoeller, H.; Cho, J.; Park, S. Effect of Oxidation on Indium Solderability. *J. Electron. Mater.* **2008**, *37*, 483−489.

(26) Lucovsky, G.; Mooradian, A.; Taylor, W.; Wright, G. B.; Keezer, R. C. Identification of the Fundamental Vibrational Modes of Trigonal, α-monoclinic and Amorphous Selenium. *Solid State Commun.* **1967**, *5*, 113−117.

(27) Chen, Y.-Z.; Liu, T.-H.; Chen, C.-Y.; Liu, C.-H.; Chen, S.-Y.; Wu, W.-W.; Wang, Z. L.; He, J.-H.; Chu, Y.-H.; Chueh, Y.-L. Taper PbZr0.2Ti0.8O3 Nanowire Arrays: From Controlled Growth by Pulsed Laser Deposition to Piezopotential Measurements. *ACS Nano* **2012**, *6*, 2826−2832.

(28) Yang, P.; Lieber, C. M. Nanostructured High-temperature Superconductors: Creation of Strong-pinning Columnar Defects in Nanorod/superconductor Composites. *J. Mater. Res.* **1977**, *12*, 2981−2996.

(29) Stach, E. A.; Pauzauskie, P. J.; Kuykendall, T.; Goldberger, J.; He, R.; Yang, P. Watching GaN Nanowires Grow. *Nano Lett.* **2003**, *3*, 867−869.

(30) Hsu, Y.-J.; Lu, S.-Y. Vapor−Solid Growth of Sn Nanowires: Growth Mechanism and Superconductivity. *J. Phys. Chem. B* **2005**, *109*, 4398−4403.

(31) Yin, Y.; Zhang, G.; Xia, Y. Synthesis and Characterization of MgO Nanowires Through a Vapor-Phase Precursor Method. *Adv. Funct. Mater.* **2002**, *12*, 293−298.

(32) Huang, M. H.; Wu, Y.; Feick, H.; Tran, N.; Weber, E.; Yang, P. Catalytic Growth of Zinc Oxide Nanowires by Vapor Transport. *Adv. Mater.* **2001**, *13*, 113−116.

(33) Volmer, M.; Weber, A. Nucleus formation in supersaturated systems. *Z. phys. Chem.* **1926**, *119*, 277−301.

(34) Wang, N.; Tang, Y. H.; Zhang, Y. F.; Lee, C. S.; Lee, S. T. Nucleation and Growth of Si Nanowires From Silicon Oxide. *Phys. Rev. B* **1998**, *58*, R16024−R16026.

(35) Springholz, G.; Frank, N.; Bauer, G. The Origin of Surface Roughening in Lattice-mismatched Frank van der Merwe Type Heteroepitaxy. *Thin Solid Films* **1995**, *267*, 15−23.

(36) Shim, B. S.; Chen, W.; Doty, C.; Xu, C.; Kotov, N. A. Smart Electronic Yarns and Wearable Fabrics for Human Biomonitoring Made by Carbon Nanotube Coating with Polyelectrolytes. *Nano Lett.* **2008**, *8*, 4151−4157.

DOI: 10.1021/acsami.8b11676
ACS Appl. Mater. Interfaces 2018, 10, 35477−35486

(37) Gent, A. N.; Lin, C. W. Model Studies of the Effect of Surface Roughness and Mechanical Interlocking on Adhesion. *J. Adhes.* **1990**, *32*, 113−125.
(38) Larsson, M. P.; Syms, R. R. A.; Wojcik, A. G. Improved Adhesion in Hybrid Si-polymer MEMS via Micromechanical Interlocking. *J. Micromech. Microeng.* **2005**, *15*, No. 2074.
(39) Rahmawan, Y.; Kang, S. M.; Lee, S. Y.; Suh, K. Y.; Yang, S. Enhanced Shear Adhesion by Mechanical Interlocking of Dual-Scaled Elastomeric Micropillars With Embedded Silica Particles. *Macromol. React. Eng.* **2013**, *7*, 616−623.
(40) Chen, Q.; Sheng, W.; Lian-Mao, P. Establishing Ohmic Contacts for in situ Current−Voltage Characteristic Measurements on a Carbon Nanotube inside the Scanning Electron Microscope. *Nanotechnology* **2006**, *17*, 1087−1098.
(41) Youngblood, N.; Chen, C.; Koester, S. J.; Li, M. Waveguide-integrated Black Phosphorus Photodetector with High Responsivity and Low Dark Current. *Nat. Photonics* **2015**, *9*, 247−252.
(42) Zhou, X.; Yang, D.; Ma, D. Extremely Low Dark Current, High Responsivity, All-Polymer Photodetectors with Spectral Response from 300 nm to 1000 nm. *Adv. Opt. Mater.* **2015**, *3*, 1570−1576.
(43) Yu, P.; Yu, X.; Lu, W.; Lin, H.; Sun, L.; Du, K.; Liu, F.; Fu, W.; Zeng, Q.; Shen, Z.; Jin, C.; Wang, Q. J.; Liu, Z. Fast Photoresponse from 1T Tin Diselenide Atomic Layers. *Adv. Funct. Mater.* **2016**, *26*, 137−145.
(44) An, B. W.; Shin, J. H.; Kim, S.-Y.; Kim, J.; Ji, S.; Park, J.; Lee, Y.; Jang, J.; Park, Y.-G.; Cho, E.; Jo, S.; Park, J.-U. Smart Sensor Systems for Wearable Electronic Devices. *Polymers* **2017**, *9*, No. 303.
(45) Yoon, J.; Baca, A. J.; Park, S.-I.; Elvikis, P.; Geddes Iii, J. B.; Li, L.; Kim, R. H.; Xiao, J.; Wang, S.; Kim, T.-H.; Motala, M. J.; Ahn, B. Y.; Duoss, E. B.; Lewis, J. A.; Nuzzo, R. G.; Ferreira, P. M.; Huang, Y.; Rockett, A.; Rogers, J. A. Ultrathin Silicon Solar Microcells for Semitransparent, Mechanically Flexible and Microconcentrator Module Designs. *Nat. Mater.* **2008**, *7*, 907−915.
(46) Chang, C.-Y.; Cheng, Y.-J.; Hung, S.-H.; Wu, J.-S.; Kao, W.-S.; Lee, C.-H.; Hsu, C.-S. Combination of Molecular, Morphological, and Interfacial Engineering to Achieve Highly Efficient and Stable Plastic Solar Cells. *Adv. Mater.* **2012**, *24*, 549−553.
(47) Efimenko, K.; Rackaitis, M.; Manias, E.; Vaziri, A.; Mahadevan, L.; Genzer, J. Nested Self-similar Wrinkling Patterns in Skins. *Nat. Mater.* **2005**, *4*, 293−297.
(48) Huck, W. T. S. Hierarchical Wrinkling. *Nat. Mater.* **2005**, *4*, 271−272.
(49) Park, J.; Kim, J.; Kim, S.-Y.; Cheong, W. H.; Jang, J.; Park, Y.-G.; Na, K.; Kim, Y.-T.; Heo, J. H.; Lee, C. Y.; Lee, J. H.; Bien, F.; Park, J.-U. Soft, Smart Contact Lenses with Integrations of Wireless Circuits, Glucose Sensors, and Displays. *Sci. Adv.* **2018**, *4*, No. eaap9841.
(50) Hu, X.; Zhang, X.; Liang, L.; Bao, J.; Li, S.; Yang, W.; Xie, Y. High-Performance Flexible Broadband Photodetector Based on Organolead Halide Perovskite. *Adv. Funct. Mater.* **2014**, *24*, 7373−7380.
(51) Tao, Y.; Wu, X.; Wang, W.; Wang, J. Flexible Photodetector from Ultraviolet to Near Infrared Based on a SnS2 Nanosheet Microsphere Film. *J. Mater. Chem. C* **2015**, *3*, 1347−1353.
(52) Sun, Z.; Liu, Z.; Li, J.; Tai, Ga; Lau, S. P.; Yan, F. Infrared Photodetectors Based on CVD-Grown Graphene and PbS Quantum Dots with Ultrahigh Responsivity. *Adv. Mater.* **2012**, *24*, 5878−5883.
(53) Benkhedir, M. L.; Aida, M. S.; Adriaenssens, G. J. Defect Levels in the Band Gap of Amorphous Selenium. *J. Non-Cryst. Solids* **2004**, *344*, 193−198.

DOI: 10.1021/acsami.8b11676
ACS Appl. Mater. Interfaces 2018, 10, 35477−35486